SCIENCE CHINA
Physics, Mechanics & Astronomy

• Article •

August 2023 Vol. 66 No. 8: 284211
https://doi.org/10.1007/s11433-023-2145-6

Chip-scale spontaneous quasi-phase matched second harmonic generation in a micro-racetrack resonator

Tingge Yuan[1], Jiangwei Wu[1], Yi'an Liu[1], Xiongshuo Yan[1], Haowei Jiang[1], Hao Li[1], Zhaokang Liang[1], Qiang Lin[3], Yuping Chen[1*], and Xianfeng Chen[1,2]

[1] *State Key Laboratory of Advanced Optical Communication Systems and Networks, School of Physics and Astronomy, Shanghai Jiao Tong University, Shanghai 200240, China;*
[2] *Collaborative Innovation Center of Light Manipulations and Applications, Shandong Normal University, Jinan 250358, China;*
[3] *Department of Electrical and Computer Engineering, University of Rochester, New York 14627, USA*

Received April 13, 2023; accepted May 22, 2023; published online July 4, 2023

In this paper, we demonstrate efficient spontaneous quasi-phase matched (SQPM) second harmonic generation (SHG) in a micro-racetrack resonator on X-cut thin film lithium niobate. Our approach does not involve poling, but exploits the anisotropy of the crystals to allow the phase-matching condition to be fulfilled spontaneously as the TE-polarized light circulates in a specifically designed racetrack resonator. In experiment, normalized on-chip conversion efficiencies of 1.01×10^{-4}/W and 0.43×10^{-4}/W are achieved by 37th-order and 111th-order SQPM, respectively. The configurable SQPM will benefit the application of nonlinear frequency conversion and quantum source generation in chip-scale integrated photonics compatible with standard CMOS fabrication processes.

lithium niobate on insulator, quasi-phase matching, second harmonic generation

PACS number(s): 42.65.-k, 42.70.Mp, 42.60.Da

Citation: T. Yuan, J. Wu, Y. Liu, X. Yan, H. Jiang, H. Li, Z. Liang, Q. Lin, Y. Chen, and X. Chen, Chip-scale spontaneous quasi-phase matched second harmonic generation in a micro-racetrack resonator, Sci. China-Phys. Mech. Astron. **66**, 284211 (2023), https://doi.org/10.1007/s11433-023-2145-6

1 Introduction

As the most fundamental nonlinear optical phenomena, second-order nonlinear parametric processes have attracted a great deal of interest since the laser was invented in the 1960s. They have been developed into a powerful tool for generating various non-classical light sources, such as entangled photon pairs [1-3] and squeezed light [4, 5] in quantum photonic networks, and more generally to provide a flexible frequency conversion to transfer the quantum state of light between different wavelengths [6, 7]. The phase-matching condition is necessary to achieve a high-efficiency nonlinear interaction [8]; however, perfect fulfilment of this normally requires strict conditions on both the dispersion property of the nonlinear medium and the orientation of the crystal axis. Quasi-phase matching (QPM) is another approach to achieving effective nonlinear interactions [9, 10] beyond birefringent phase matching [8]. It requires the sign or magnitude of the second-order nonlinear susceptibility to be periodically modulated, thus the phase mismatch between the interacting waves can be intermittently compensated and the intensity of the newly generated frequency component will grow continuously. To date, the most common and mature approach to constructing a QPM

*Corresponding author (email: ypchen@sjtu.edu.cn)

structure is electric-field-induced ferroelectric domain inversion, (i.e., electric field poling [11, 12]), via which the sign of the nonlinear susceptibility can be totally inverted. However, this method requires the prefabrication of the electrode and high-voltage field, leading to a complex fabrication procedure with large cost. Furthermore, in the area of the chip-scale integrated photonics, the CMOS-incompatible electric field poling process will hinder the large-scale production of integrated quantum photonic circuits with the QPM devices. To fully explore the potential of wafer-scale quantum photonic chips, there is an urgent need to find a novel approach to the integrated QPM devices compatible with the standard CMOS fabrication processes.

In the past decades, various chip-integrated photonic elements have been reported [13-16], in which high-quality whispering gallery mode micro-resonator has emerged as a promising platform of optical nonlinear interactions due to the significant enhancement of the light-material interactions [17-25]. Thanks to the circular property of the light traveling in the WGM micro-resonator, a crystal-anisotropy induced poling-free QPM mechanism has been proposed in the asymmetric crystalline resonator, based on which the effective second-order nonlinear susceptibility d_{eff} can be modulated naturally as the light propagates around the optical axis. Such orientation based mechanism has firstly been implemented on the $\bar{4}$ symmetry materials (known as $\bar{4}$ QPM) [26-28]. Recently, a broadband natural QPM harmonic generation has also been achieved in a micro-disk resonator on lithium niobate (LN) [29-31]. However, limited by the circular geometry, only first-order QPM is available with the continuously modulated d_{eff} [32]. Until now, there still lacks of reports on specifically controlled natural QPM on LN, and the huge potential of the orientation induced natural domain inversion is unrevealed.

In this paper, we propose and demonstrate the micro-racetrack resonator based spontaneous quasi phase matching (SQPM) on X-cut thin-film lithium niobate (TFLN). Compared with the previous work using micro-disk or micro-ring resonator, racetrack structure provides great flexibility in the choice of the different QPM conditions from the first to the high-order, and meanwhile, features lots of advantages such as the full utilization of the largest d_{33}, a large mode overlap by using the fundamental modes. As a result, high-efficiency nonlinear frequency conversion can be achieved in a racetrack resonator without external steps for domain inversion. In experiments, both the 37th-order and 111th-order SQPM racetrack resonator have been fabricated on X-cut TFLN, and an SQPM induced second harmonic generation (SHG) with normalized on-chip conversion efficiency of 1.01×10^{-4}/W and 0.43×10^{-4}/W is observed, respectively. Theoretical predictions indicate that the on-chip conversion efficiency can be further improved to about 4000%/W by using the first-order SQPM and the critical coupling condition. In addition to the example presented in this work, SQPM can be employed for other second-order nonlinear frequency conversion processes, such as spontaneous parametric down-conversions, optical parametric oscillations, and even the generation of micro-frequency combs, which will promote the application of integrated nonlinear photonics in both the classical and quantum regimes.

2 Principle

LN is an outstanding optical material due to its huge second-order nonlinear susceptibility and the capability of being poled [33-36]. With the assistance of QPM technology, periodically poled lithium niobate (PPLN) can be used to realize the ultra-high efficiency of the nonlinear frequency conversion process [37-40]. As a result, we choose the LN based SQPM as a typical example, and show how we can achieve a similar result of QPM SHG in a poling-free way. As Figure 1(a) has shown, under the traditional configuration of QPM based on the electric field poling, the domain orientation (i.e., the $+Z$-axis of LN) is periodically inverted along the propagation direction of the light with a period of Λ. For the phase-matching condition, Λ should satisfy the relationship:

$$\Lambda = \frac{2\pi m}{\Delta k} = 2mL_{\text{c}}, \tag{1}$$

where m is a positive odd, representing the order of the QPM. Δk is the phase mismatch in the nonlinear interaction, and L_{c} is the coherent length. This traditional mechanism for QPM can be summarized as a periodically inverted domain and an unchanged direction of propagation for the light. While considering the relative angular relationship between the wave-vector and crystal axis, an equivalent result can be obtained if the propagation direction of light is periodically reversed, and this poling-free scheme will be practically realized by forming a micro-racetrack resonator on X-cut LN, just like Figure 1(b) and (c) have depicted.

Here, we define θ as the azimuthal angle between the wave vector $\mathbf{k}$ and the Z-axis in Figure 1(d). To meet the QPM condition, the straight section of the racetrack should be placed perpendicular to the Z-axis of the LN, and both the straight waveguide length L_0 and half-circle radius R should be carefully designed to satisfy following equations:

$$L_0 = mL_{\text{c}}, \tag{2a}$$

$$\Delta\phi = \int_0^{2\pi} \Delta k(\theta) R \mathrm{d}\theta = N2\pi, \tag{2b}$$

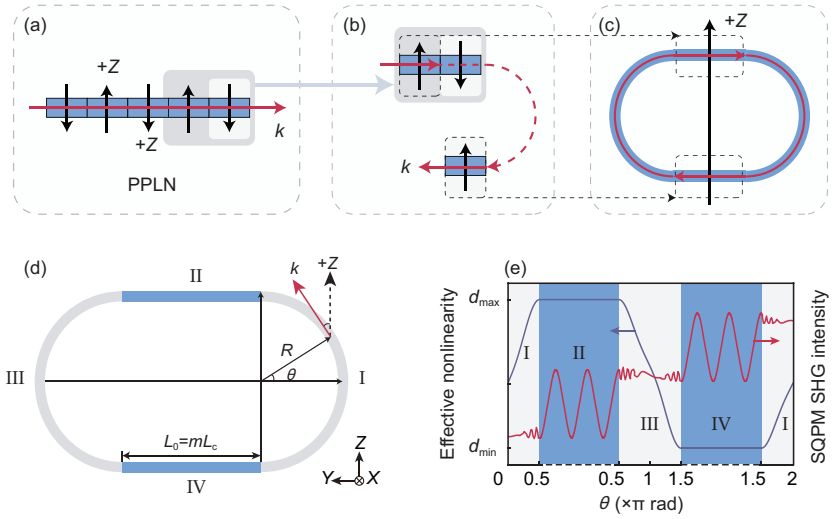

Figure 1 (Color online) Principle of the racetrack resonator based SQPM. (a) Traditional approach to QPM using PPLN; (b) naturally inversed domain dependent on the propagation direction; (c) racetrack resonator with spontaneously inversed domain as the light circulates in the resonator; (d) the schematic diagram of azimuth angle θ in micro-racetrack resonator; (e) the relationship between effective nonlinear coefficient and SHG intensity with θ in a 5th-order SQPM racetrack resonator. Noted that θ will keep constant in the straight waveguide since the unvarying propagation direction of the light.

where $\Delta\phi$ is the phase-mismatch delay in the half-circle waveguide, which is limited to $N2\pi$ to ensure that the phase relationship between two straights have not been interrupted. For the TE-polarized interacting waves in a nonlinear process, the effective nonlinear coefficient along the path once the light travels around the racetrack resonator is given by

$$d_{\text{eff}}(\theta) = -d_{22}\cos^3\theta + d_{31}\cos^2\theta\sin\theta + d_{33}\sin^3\theta. \quad (3)$$

Each time the light travels from one of the straight waveguide to another, d_{eff} will oscillate between the maximum and the minimum, which can be approximated as d_{33} and $-d_{33}$, as the blue curve in Figure 1(e) has shown. Meanwhile, for the most fundamental SHG process, the variation of the generated harmonic wave within an SQPM period has also been displayed. It can be seen from the red curve that in the straight waveguide (represented by the blue region), the SH intensity experiences a rapid oscillation, but finally tends to grow in the adjacent waveguide due to the inversed d_{eff}; while in the half-circle waveguides (represented by the white region), the absolute value of d_{eff} quickly decreases to 0 where the sign reverses, and then increases to the next maximum. Corresponding oscillation of SH intensity follows the same tendency, and the overall intensity change in this section can be approximated to 0. As a result, conversion efficiency in an SQPM racetrack resonator is dependent on the geometric structure, which will be discussed in the following sections.

3 Design and fabrication

To demonstrate the effect of SQPM, we designed a micro-racetrack resonator for SHG with a fundamental wave (FW) wavelength at C-band, and both the FW and second harmonic wave (SH) are in the TE_{00} mode to employ the largest mode overlap and the largest nonlinear coefficient d_{33}. The thickness h of the TFLN we used here is 0.6 μm, and the side-wall angle α of the ridge waveguide is specified as 60° due to the previous fabrication experience.

We started the design with the half-circle waveguides firstly, and carried the modal analysis of the curved waveguide with the conformal transformation [41], which is usually used to transform the the curved waveguide with the uniform distributed index to an equivalent straight one with the graded distributed index, as Figure 2(a) has illustrated, so that the effective refractive index in the curved waveguide can be derived from the mode in the transformed cross section (details can be found in Appendix A1). In our case, material index in the half-circle waveguide varies with θ due to birefringence of LN, so that the half-circle waveguide was dissolved into tiny curved sections with specific extraordinary refractive index. By performing conformal transformation on each one and calculating the effective refractive indices, phase delays of the FW and SH were finally obtained by summing them up. In fact, besides the outside radius R_2, cross section geometry of the waveguide also has a difference to phase delays. We optimized these parameters based on the single-mode condition and the integer condition for phase delay, and finally determined the top width W and the waveguide thickness t as 1 and 0.38 μm, respectively. Figure 2(b) shows the result calculated based on above structure. As R_2 = 129.03 μm, total phase delays of both FW and SH in a pair of half-circle waveguides equal even multiples of 2π,

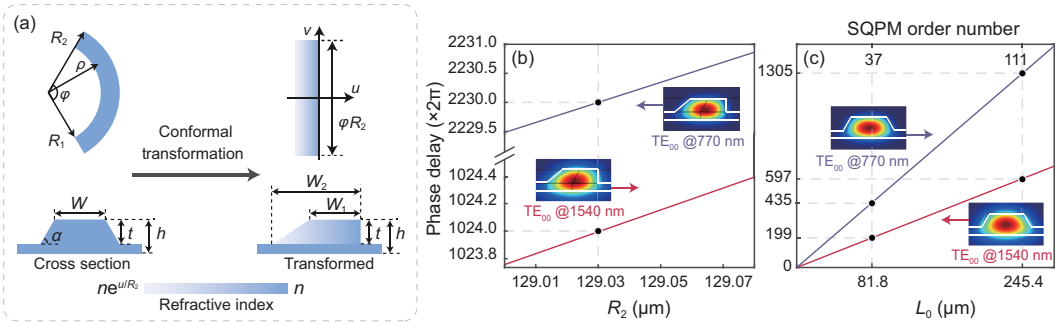

Figure 2 (Color online) (a) Schematic of conformal transformation used for mode analysis of the curved waveguide. Calculated total phase delays of FW and SH in a pair of (b) half-circle waveguides and (c) straight waveguides.

corresponding to a phase-mismatch delay $\Delta\phi = 91 \times 2\pi$ in a single half-circle waveguide.

Based on the determined waveguide cross section, effective refractive indices at FW and SH, as well as the coherent length in the straight waveguide were directly calculated, as the insets show in Figure 2(c). Furthermore, to ensure the resonance condition of interacting waves in the racetrack resonator, total phase delays of FW and SH in a pair of straight waveguides should equal integer multiples of 2π at the same time since we have designed the half-circle waveguide to meet the same integer-multiple 2π condition at FW and SH. Here, effective refractive indices are calculated to be approximately 1.8732 for FW and 2.0472 for SH, respectively, and the coherent length L_c is about 2.21 μm. As Figure 2(c) has indicated, when L_0 equals 81.8 and 245.4 μm, both the resonance and QPM condition can be satisfied simultaneously, corresponding to the SQPM order number of 37 and 111.

Finally, a pulley coupling waveguide [42] and a pair of grating couplers were designed for coupling. To maximize the coupling efficiency of the TE_{00} mode for the FW band, the width of the coupling waveguide and the gap between the waveguide and resonator were designed to be 0.6 and 0.8 μm, respectively, and the central angle was 30°.

Figure 3(a) illustrates the fabrication process of the micro-racetrack resonator. Amorphous silicon thin film was deposited on TFLN as a hard mask by plasma-enhanced chemical vapor deposition (PECVD). The racetrack patterns were defined in ZEP520A resist using standard electron beam lithography. The patterns were first transferred into the hard mask by reactive ion etching (RIE) with sulfur hexauoride (SF6). Subsequently, the patterns were transferred into the LN film using inductively coupled plasma-reactive ion etching (ICP-RIE) with Argon (Ar). Finally, RCA cleaning was performed to remove the hard mask and small particles. Figure 3(b)-(d) show the optical and scanning electron microscopy images of the fabricated micro-racetrack resonator, where the LN film was etched to a total depth of 380 nm, leaving a slab of 220 nm, fitting well with our design.

4 Experiment and result

In this section, SQPM SHG is experimentally demonstrated. Figure 4(a) shows experimental setup. An infrared tunable laser (New Focus TLB-6728) served as the laser source of FW. The input laser was first amplified by an erbium-doped optical fibre amplifier (EDFA), and then adjusted by a polarization controller (PC). At the output port, the FW and SH were separated by a wavelength division multiplexer (WDM). A photodetector (PD) connected to an oscilloscope (OSC) was used to record the transmission spectrum of the FW, while an optical spectrum analyser (OSA) was used to measure the SH signal.

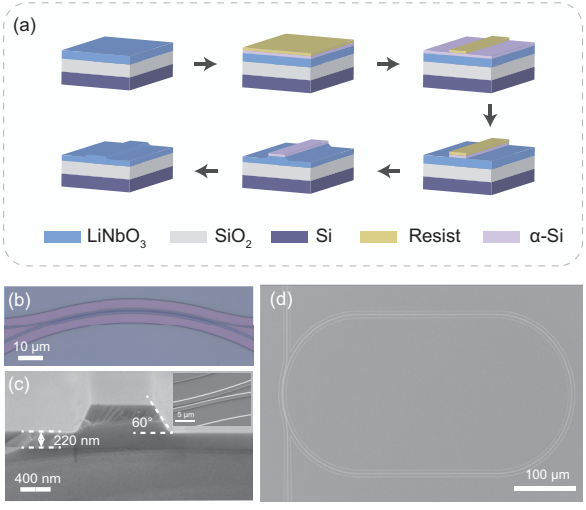

Figure 3 (Color online) (a) Fabrication process of the micro-racetrack resonator; (b) optical microscopic image of the pulley coupling waveguide; (c) cross section, coupling region; (d) the top view of the fabricated micro-racetrack resonator under a scanning electron microscope.

In our experiment, the linear properties of the 37th-order and 111th-order (SQPM) racetrack resonator were characterized at first. As the transmission spectrum in Figure 4(b1) and (b2) has shown, the free spectrum range (FSR) of the 37th-order racetrack resonator is larger than that of the 111th-order one due to the relatively shorter straight waveguide length, while its loaded quality (Q) factor (24.5k) is lower than that (31.6k) in the 111th-order racetrack resonator, which can be obviously seen from the Lorentzian fits in Figure 4(c1) and (c2). In addition, coupling conditions for these two racetrack resonator are different as well. In the 37th-order one, the FW light is mainly in the under-coupling condition, while in the 111th-order one, the light is slightly over coupled. The grating coupling efficiencies at FW band and SH band are about 6 and 17.9 dB/facet, respectively. Due to the relatively low coupling efficiency of the SH, no efficient transmission spectrum at SH was recorded.

In the next, we amplified the C-band laser to hundreds of milliwatts, and tuned the wavelength searching for the SHG signal on OSA. With the optimized grating coupling condition, we found the highest SH signal at 770.1 nm appearing when the FW wavelength was around 1540.2 nm in both the 37th-order and 111th-order racetrack resonator, as Figure 5(a1) and (a2) have shown. The normalized SH intensity in the adjacent FW resonant modes has also been recorded. The envelopes of the SHG spectrum are depicted by the dashed curves, which show FWHMs of 1.2 and 1.5 nm, respectively, corresponding to the bandwidths of 37th- and 111th-order SQPM SHG. Figure 5(b1) and (b2) show the OSA recorded SH profiles with the FW wavelength fixed at 1540.2 nm, and the intensities have been normalized to the maximum of that in the 37th-order SQPM SHG. With the on-chip FW light launched at the same power of 22.3 mW, the SH intensity in the 37th-order racetrack resonator is about two times higher

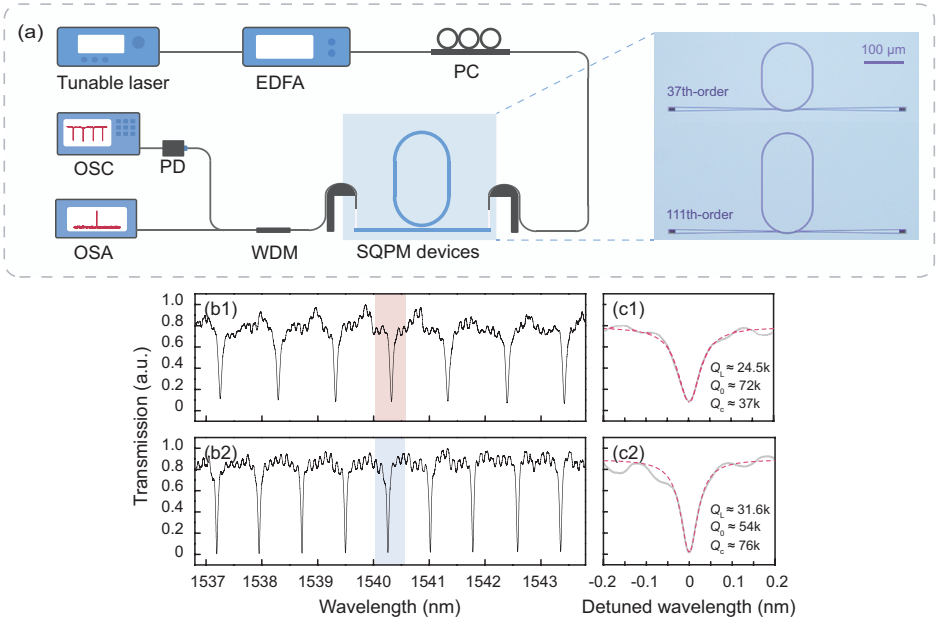

Figure 4 (Color online) (a) Experimental setup. Inset: 37th-order and 111th-order SQPM racetracks under an optical microscope. (b1), (b2) Recorded transmission spectrum; (c1), (c2) corresponding Lorentzian fits of the marked dips in the 37th-order and 111th-order SQPM racetrack resonator, respectively.

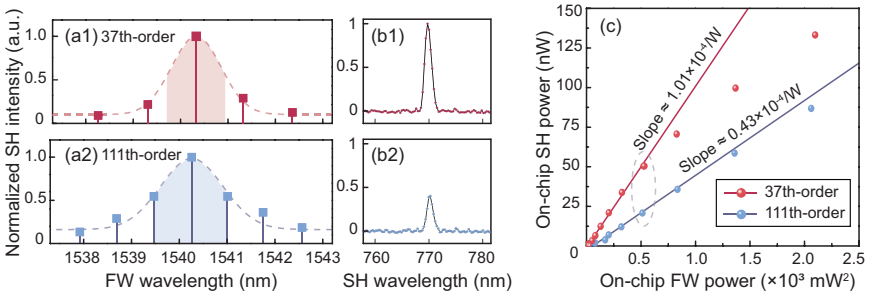

Figure 5 (Color online) (a1), (a2) Measured SH intensity pumped by different resonant modes of FW; (b1), (b2) SH profiles detected by OSA with the FW wavelength at 1540.2 nm; (c) on-chip SH power versus square of the on-chip FW power. The dots in the dashed ellipse correspond to the peaks in (b1), (b2).

than that in the 111th-order one.

At last, SH power was measured versus the increasing input FW power in two resonators with the FW wavelength fixed to obtain the highest SH output, and the results are shown in Figure 5(c), where the dots and lines indicate the experimental data and linear fits, respectively. The calculated on-chip conversion efficiency of SHG is about 1.01×10^{-4}/W by 37th-order SQPM and 0.43×10^{-4}/W by 111th-order SQPM. As the FW power increases, the measured data begin to deviate from linearity in the 37th-order one, which may be attributed to the thermal detuning of FW.

5 Discussion

It is noteworthy that due to the relatively narrow waveguide width designed in this work, no modal phase matching [43, 44] nor cyclic phase matching [45, 46] between higher-order modes could occur in our racetrack resonator, thus the only mechanism in charge of the SHG is SQPM. This fact can also be evidenced by the difference in conversion efficiencies enabled by the 37th-order SQPM and 111th-order SQPM. However, due to the environmental difference and fabrication error, the resonant mode may miss the central wavelength in the SHG spectrum, as the dashed blue curve in Figure 6(a) has shown. Such asymmetrical SH intensity distribution around the central FW mode is also revealed by the measured SH spectrum in the 37th-order racetrack resonator in Figure 5(a1). To further enhance the conversion efficiency, additional thermo-optic or electro-optic modulation can be applied to finely tune the relative position between the resonant mode and SHG spectrum.

Conversion efficiency of the SQPM racetrack resonator also depends on the resonator structure and the coupling condition of interacting waves. With the undepleted pump approximation and the coupled mode equation, on-chip conversion efficiency of SHG in an SQPM micro-racetrack resonator can be derived as $\eta_{on} = \eta'_{on} f_2 {f_1}^2$ (see in the Appendix A2) [47], with

$$\eta'_{on} = \frac{4096 {d_{33}}^2 {L_c}^2 {Q_{l,2}}^2 {Q_{l,1}}^4 \xi}{\varepsilon_0 c n_2 {n_1}^2 {\lambda_1}^2 \pi^3 Q_{c,2} {Q_{c,1}}^2 (m_2 + M_2)(m_1 + M_1)^2}, \tag{4}$$

$$f_{1,(2)} = \frac{\pi^2 c^2}{\pi^2 c^2 + {\Delta_{1(2)}}^2 {\lambda_{1(2)}}^2 {Q_{l,1(2)}}^2}. \tag{5}$$

Here, η'_{on} denotes the ideal dual-resonant on-chip conversion efficiency. The subscript 1 represents the FW and 2 represents the SH. $Q_{l,1(2)}$ and $Q_{c,1(2)}$ are loaded and coupling Q factor, respectively. $n_{1(2)}$ is the effective refractive index in the straight waveguide. $\lambda_{1(2)}$ is the vacuum wavelength. $m_{1(2)}$ is the azimuthal mode number in the curved section, and $M_{1(2)}$ is that in the straight section. In our design, as shown in Figure 2(b) and (c), $m_1 = 1024$, $m_2 = 2230$. For the 37th-order racetrack resonator, $M_1 = 199$, $M_2 = 435$; for the 111th-order racetrack resonator, $M_1 = 597$, $M_2 = 1305$. ξ is the mode overlap factor. $f_{1,(2)}$ is a function related to the resonant condition of the FW(SH), in which $\Delta_{1(2)}$ is the detuning of the FW(SH) frequency from the resonance. Once $\Delta_{1(2)} = 0$ is achieved, dual-resonant on-chip conversion efficiency $\eta_{on} = \eta'_{on}$ is obtained.

Different from the conversion efficiency in the traditional PPLN waveguide which is inverse to the square of the QPM order at a given length, conversion efficiency obtained by different-order SQPM relies on circumference of the racetrack resonator, i.e., $(m_2 + M_2)(m_1 + M_1)^2$, which means for the 37th-order and 111th-order SQPM racetrack resonator in our experiment, the ratio of their on-chip conversion efficiencies is theoretically 2.33 if the other parameters are the same. However, as we have shown before, both the Q factor and the coupling condition of FW in the 111th-order racetrack resonator are better than that in the 37th-order one, which will make this two efficiencies closer. Here, we assume in our ex-

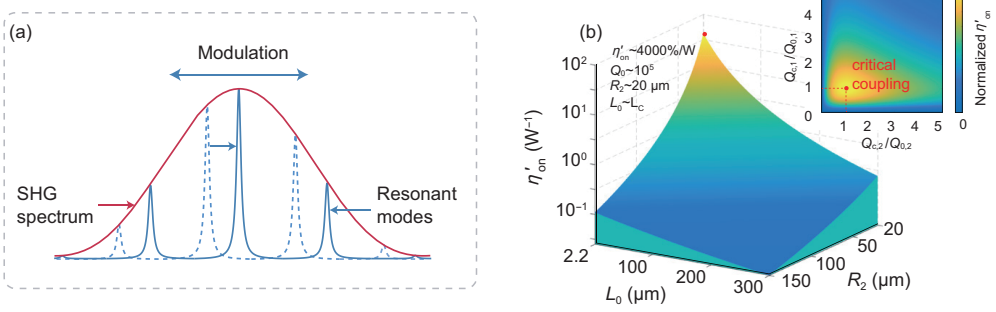

Figure 6 (Color online) (a) Applying modulation to meet the perfect match between the central FW wavelength in the SHG spectrum and the resonant condition; (b) theoretical prediction of the dual-resonant on-chip conversion efficiency with varying R_2 and L_0 (SQPM order) in log scale. Inset: normalized dual-resonant on-chip conversion efficiency versus different coupling conditions of FW and SH.

periment, the intrinsic Q factors in these two resonators at SH are 10^4, and the coupling conditions (Q_c/Q_0) are as the same as that at FW. Based on eq. (4), the theoretically predicted on-chip conversion efficiency is about 4.32×10^{-4}/W for the 37th-order SQPM, and 3.09×10^{-4}/W for the 111th-order SQPM, which are a bit higher, but still close to the measured results.

Furthermore, we consider the intrinsic Q factors for both the FW and SH reach 10^5, and Q_c is modulated by changing the gap and the length of the coupling region. Figure 6(b) shows the dual-resonant on-chip conversion efficiency η'_{on} versus different geometrical parameters and the coupling conditions. As the inset has indicated, the optimized coupling condition is achieved when the critical coupling is realized for FW and SH, based on which a ultra-high on-chip conversion of about 4000%/W is obtained with a minimum radius of 20 μm and a minimum straight waveguide length of L_c, using the first-order SQPM. And it is expected to be higher with an improved Q factor, which can be realized by improving the fabrication process or optimizing the structure of the curved waveguide [48].

In fact, varying geometrical parameters will also influence the phase-matching and resonant condition, thus the realistic conversion efficiency in Figure 6(b) should be a series of peaks instead of a smooth surface. However, it still reveals a huge potential of SQPM in the nonlinear frequency conversion on integrated photonics platform, especially when the fabrication accuracy and simulation precision are improved in the future.

6 Conclusions

In this paper, we have theoretically and experimentally demonstrated an SQPM SHG in a fully integrated micro-racetrack resonator on X-cut TFLN based on dispersion engineering and the design of the crystal orientation. On-chip conversion efficiencies of 1.01 $\times 10^{-4}$/W and 0.43 $\times 10^{-4}$/W have been obtained in a 37th-order SQPM resonator and a 111th-order SQPM resonator, respectively. The conversion efficiency could be further improved by optimizing the racetrack structure, improving the resonator Q-factor, or applying thermo-optic or electro-optic modulation to realize the perfect match of the resonance mode and the central FW wavelength. Theoretical analysis indicates that by using the first-order QPM and the critical coupling, on-chip conversion efficiency could reach 4000%/W with an intrinsic Q factor of 10^5. This novel approach to achieve a chip-scale efficient nonlinear frequency conversion process is compatible with the standard CMOS fabrication processes, and is suitable for large-scale production of integrated photonic chips. By designing the racetrack structures to compensate for different kinds of phase mismatching, SQPM can be employed for almost all second-order nonlinear optical processes, which will be valuable in terms of fabricating integrated quantum light sources or other nonlinear photonic elements on integrated photonic circuit.

This work was supported by the National Key R&D Program of China (Grant No. 2019YFB2203501), National Natural Science Foundation of China (Grant Nos. 12134009, and 91950107), Shanghai Municipal Science and Technology Major Project (Grant No. 2019SHZDZX01-ZX06), and Shanghai Jiao Tong University (SJTU) (Grant No. 21X010200828).

1 C. Kurtsiefer, M. Oberparleiter, and H. Weinfurter, Phys. Rev. A **64**, 023802 (2001).
2 R. Luo, H. Jiang, S. Rogers, H. Liang, Y. He, and Q. Lin, Opt. Express **25**, 24531 (2017).
3 Z. Ma, J. Y. Chen, Z. Li, C. Tang, Y. M. Sua, H. Fan, and Y. P. Huang, Phys. Rev. Lett. **125**, 263602 (2020).
4 L. A. Wu, H. J. Kimble, J. L. Hall, and H. Wu, Phys. Rev. Lett. **57**, 2520 (1986).
5 X. Guo, C. Zou, C. Schuck, H. Jung, R. Cheng, and H. X. Tang, Light Sci. Appl. **6**, e16249 (2017).
6 P. Kumar, Opt. Lett. **15**, 1476 (1990).
7 M. G. Raymer, and K. Srinivasan, Phys. Today **65**, 32 (2012).
8 R. W. Boyd, *Nonlinear Optics* (Academic Press, Singapore, 2020).
9 J. A. Armstrong, N. Bloembergen, J. Ducuing, and P. S. Pershan, Phys. Rev. **127**, 1918 (1962).
10 P. A. Franken, and J. F. Ward, Rev. Mod. Phys. **35**, 23 (1963).
11 S. Zhu, Y. Zhu, and N. Ming, Science **278**, 843 (1997).
12 M. M. Fejer, G. A. Magel, D. H. Jundt, and R. L. Byer, IEEE J. Quantum Electron. **28**, 2631 (1992).
13 C. Wang, M. Zhang, X. Chen, M. Bertrand, A. Shams-Ansari, S. Chandrasekhar, P. Winzer, and M. Lončar, Nature **562**, 101 (2018).
14 M. He, M. Xu, Y. Ren, J. Jian, Z. Ruan, Y. Xu, S. Gao, S. Sun, X. Wen, L. Zhou, L. Liu, C. Guo, H. Chen, S. Yu, L. Liu, and X. Cai, Nat. Photon. **13**, 359 (2019).
15 M. Li, J. Ling, Y. He, U. A. Javid, S. Xue, and Q. Lin, Nat. Commun. **11**, 4123 (2020).
16 Y. A. Liu, X. S. Yan, J. W. Wu, B. Zhu, Y. P. Chen, and X. F. Chen, Sci. China-Phys. Mech. Astron. **64**, 234262 (2021).
17 K. J. Vahala, Nature **424**, 839 (2003).
18 G. Lin, A. Coillet, and Y. K. Chembo, Adv. Opt. Photon. **9**, 828 (2017).
19 I. Breunig, Laser Photonics Rev. **10**, 569 (2016).
20 Q. Mo, S. Li, Y. Liu, X. Jiang, G. Zhao, Z. Xie, X. Lv, and S. Zhu, Chin. Opt. Lett. **14**, 091902 (2016).
21 H. Wang, Y. K. Lu, L. Wu, D. Y. Oh, B. Shen, S. H. Lee, and K. Vahala, Light Sci. Appl. **9**, 205 (2020).
22 J. Liu, F. Bo, L. Chang, C. H. Dong, X. Ou, B. Regan, X. Shen, Q. Song, B. Yao, W. Zhang, C. L. Zou, and Y. F. Xiao, Sci. China-Phys. Mech. Astron. **65**, 104201 (2022).
23 J. Chen, X. Shen, S. J. Tang, Q. T. Cao, Q. Gong, and Y. F. Xiao, Phys. Rev. Lett. **123**, 173902 (2019).
24 X. Zhang, Q.-T. Cao, Z. Wang, Y. X. Liu, C. W. Qiu, L. Yang, Q. Gong, and Y.-F. Xiao, Nat. Photon. **13**, 21 (2018).
25 Y. F. Xiao, and F. Vollmer, Light Sci. Appl. **10**, 141 (2021).
26 P. S. Kuo, J. Bravo-Abad, and G. S. Solomon, Nat. Commun. **5**, 3109 (2014).
27 S. Mariani, A. Andronico, A. Lemaître, I. Favero, S. Ducci, and G. Leo, Opt. Lett. **39**, 3062 (2014).
28 D. P. Lake, M. Mitchell, H. Jayakumar, L. F. dos Santos, D. Curic, and P. E. Barclay, Appl. Phys. Lett. **108**, 031109 (2016).

29 J. Lin, N. Yao, Z. Hao, J. Zhang, W. Mao, M. Wang, W. Chu, R. Wu, Z. Fang, L. Qiao, W. Fang, F. Bo, and Y. Cheng, Phys. Rev. Lett. **122**, 173903 (2019).
30 B. Y. Xu, L. K. Chen, J. T. Lin, L. T. Feng, R. Niu, Z. Y. Zhou, R. H. Gao, C. H. Dong, G. C. Guo, Q. H. Gong, Y. Cheng, Y. F. Xiao, and X. F. Ren, Sci. China-Phys. Mech. Astron. **65**, 294262 (2022).
31 J. Zhu, X. Sun, T. Ding, Y. Tang, S. Liu, Y. Zheng, and X. Chen, J. Opt. Soc. Am. B **40**, D44 (2023).
32 P. S. Kuo, W. Fang, and G. S. Solomon, Opt. Lett. **34**, 3580 (2009).
33 A. Boes, B. Corcoran, L. Chang, J. Bowers, and A. Mitchell, Laser Photon. Rev. **12**, 1700256 (2018).
34 S. Saravi, T. Pertsch, and F. Setzpfandt, Adv. Opt. Mater. **9**, 2100789 (2021).
35 D. Sun, Y. Zhang, D. Wang, W. Song, X. Liu, J. Pang, D. Geng, Y. Sang, and H. Liu, Light Sci. Appl. **9**, 197 (2020).
36 J. Lin, F. Bo, Y. Cheng, and J. Xu, Photon. Res. **8**, 1910 (2020).
37 J. Y. Chen, Z. H. Ma, Y. M. Sua, Z. Li, C. Tang, and Y. P. Huang, Optica **6**, 1244 (2019).
38 J. Lu, J. B. Surya, X. Liu, A. W. Bruch, Z. Gong, Y. Xu, and H. X. Tang, Optica **6**, 1455 (2019).
39 J. Lu, M. Li, C. L. Zou, A. Al Sayem, and H. X. Tang, Optica **7**, 1654 (2020).
40 Y. Niu, L. Yang, D. Guo, Y. Chen, X. Li, G. Zhao, and X. Hu, Chin. Opt. Lett. **18**, 111902 (2020).
41 M. Heiblum, and J. Harris, IEEE J. Quantum Electron. **11**, 75 (1975).
42 E. Shah Hosseini, S. Yegnanarayanan, A. H. Atabaki, M. Soltani, and A. Adibi, Opt. Express **18**, 2127 (2010).
43 R. Luo, Y. He, H. Liang, M. Li, J. Ling, and Q. Lin, Phys. Rev. Appl. **11**, 034026 (2019).
44 X. Ye, S. Liu, Y. Chen, Y. Zheng, and X. Chen, Opt. Lett. **45**, 523 (2020).
45 J. Lin, Y. Xu, J. Ni, M. Wang, Z. Fang, L. Qiao, W. Fang, and Y. Cheng, Phys. Rev. Appl. **6**, 014002 (2016).
46 G. Lin, J. U. Fürst, D. V. Strekalov, and N. Yu, Appl. Phys. Lett. **103**, 181107 (2013).
47 B. Sturman, and I. Breunig, J. Opt. Soc. Am. B **28**, 2465 (2011).
48 M. Bahadori, M. Nikdast, Q. Cheng, and K. Bergman, J. Lightwave Technol. **37**, 3044 (2019).

Appendix A1

It is known that in a typical conformal transformation [41], the width of the transformed waveguide is defined by

$$W = R_2 \ln \frac{R_2}{R_1}, \tag{a1}$$

where R_2 and R_1 are the outside radius and inside radius of the circularly curved waveguide, respectively.

However, for the trapezoidal-shaped waveguide fabricated in our experiment, both the inside and outside radii change with different height s_0, as shown in Figure a1:

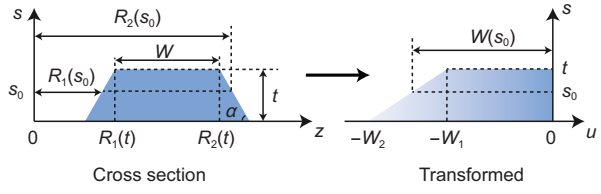

Figure a1 (Color online) Schematic of the conformal transformation for the geometry parameters in the waveguide cross section.

$$R_1(s_0) = R_2(t) - W + \frac{s_0 - t}{\tan\alpha}, \tag{a2}$$

$$R_2(s_0) = R_2(t) + \frac{t - s_0}{\tan\alpha}, \tag{a3}$$

where $R_2(t)$ is the outside radius in the top layer of the waveguide, as the same as the design parameter R_2 in the main text. W is the waveguide width, t is the waveguide thickness and α is the tilt angle. As a result, the waveguide width $W(s_0)$ corresponding to the different height s_0 after the conformal transformation can be calculated as:

$$W(s_0) = R_2(s_0) \ln \frac{R_2(s_0)}{R_1(s_0)}. \tag{a4}$$

Since the outside edge points in each layer have been transformed to share the same horizontal coordinate of 0, the inclined outside wall will turn to a straight one, while the inside wall will remain inclined. And this is why the transformed waveguide cross section has an asymmetric geometry.

Besides, conformal transformation of the refractive index follows the equation:

$$n'(u_0, s_0) = n \exp \frac{u_0}{R_2(s_0)}, \tag{a5}$$

where n' is the position dependent refractive index in the transformed waveguide and n is the material index. The calculated effective refractive index of the mode in the transformed waveguide can also be transformed back to the actual modal index using eq. (a5), where u_0 and s_0 are given by the coordinates with the maximum field intensity in the modal profile.

Appendix A2

Derivation of the on-chip conversion efficiency of an SQPM enabled SHG is based on the undepleted pump and slowing varying amplitude approximations [47]. Here, we only consider the nonlinear interaction in the straight waveguides for simplicity, and the varying SH amplitude is described by the coupled wave equation [8] as below:

$$\frac{\mathrm{d}A_{20}}{\mathrm{d}s} = -\mathrm{i}\frac{4\pi d_{\mathrm{eff}}}{n_2\lambda_1} {A_{10}}^2 \exp(\mathrm{i}\Delta k s), \tag{a6}$$

where A_{10} is the intracavity amplitude of the FW under the steady state. For m-order SQPM, the effective nonlinear coefficient has the same form of that in an PPLN like

$$d_{\mathrm{eff}} = \frac{2d_{33}}{m\pi} \exp(-\mathrm{i}k_m s), \tag{a7}$$

where $k_m = \pi/L_0$ is m-order reciprocal vector to compensate the phase-mismatch. Neglecting the coupling loss in each

loop and integrating eq. (a6) from 0 to $2L_0$, the increase of the SH amplitude peer round trip in the racetrack resonator can be calculated as:

$$\Delta A_{20} = \frac{16 d_{33} L_c {A_{10}}^2}{n_2 \lambda_1}. \tag{a8}$$

Then the intracavity conversion efficiency is derived. Considering the resonance, loss and nonlinear gain, both the FW and SH amplitude propagating in a WGM resonant with a coupling waveguide are dominated by the coupled mode equations in the time domain as:

$$\begin{cases} \dfrac{\mathrm{d}A_1}{\mathrm{d}t} = -\alpha_1 A_1 - \mathrm{i}\Delta_1 A_1 + \dfrac{A_{\mathrm{in}}}{T_1}, \\ \dfrac{\mathrm{d}A_2}{\mathrm{d}t} = -\alpha_2 A_1 - \mathrm{i}\Delta_2 A_1 + \dfrac{\Delta A_{20}}{T_2}, \end{cases} \tag{a9}$$

where $A_{1(2)}$ is the intracavity amplitude of FW(SH), $\alpha_{1(2)}$ is the total loss rate of FW(SH) in the resonator. In experiment, the Q factor is generally used to characterize the loss property of the cavity. For the total loss $\alpha = \alpha_i + \alpha_c$ which includes both the intrinsic and coupling loss terms, it can be expressed by the loaded Q factor Q_l by $\frac{1}{2}\frac{2\pi c}{\lambda Q_l}$ [47]. $\Delta_{1(2)} = \Omega_{1(2)} - \omega_{1(2)}$ is the detuning of the amplitude frequency $\omega_{1(2)}$ from the corresponding resonance frequency $\Omega_{1(2)}$. $A_1 = \kappa_1 A_{\mathrm{on1}}$ is the amplitude of FW coupled into the resonator, where κ_1 is the amplitude coupling coefficient and A_{on1} is the on-chip amplitude of FW. ΔA_{20} is the increase of the SH we calculated in the last section. $T_{1(2)}$ is the round-trip time of FW(SH), which can be calculated by $(m_{1(2)} + M_{1(2)})\lambda_{1(2)}/c$ for the racetrack resonator.

Based on eq. (a9), the steady-state amplitude of FW and SH can be solved as:

$$A_{10} = \frac{A_{\mathrm{in}}}{T_1(\alpha_1 + \mathrm{i}\Delta_1)}, \tag{a10}$$

$$A_{20} = \frac{\Delta A_{20}}{T_2(\alpha_2 + \mathrm{i}\Delta_2)}. \tag{a11}$$

Then insert expressions of ΔA_{20} and T_2 in eq. (a11), the relation between A_{20} and A_{in} can be obtained. As a result, the intracavity conversion efficiency $\eta_{\mathrm{in}} = P_{20}/{P_{\mathrm{in}}}^2$ can be derived as:

$$\eta_{\mathrm{in}} = \frac{512 {d_{33}}^2 {L_c}^2 {Q_{l,2}}^2 {Q_{l,1}}^4}{\varepsilon_0 c n_2 {n_1}^2 {\lambda_1}^2 \pi^6 (m_2 + M_2)^2 (m_1 + M_1)^4} \xi {f_2} {f_1}^2, \tag{a12}$$

with

$$\xi = \frac{(\iint {u_1}^* u_1 u_2 \mathrm{d}\sigma)^2}{(\iint |u_1|^2 \mathrm{d}\sigma)^2 \iint |u_2|^2 \mathrm{d}\sigma}, \tag{a13}$$

$$f_{1,(2)} = \frac{\pi^2 c^2}{\pi^2 c^2 + {\Delta_{1(2)}}^2 {\lambda_{1(2)}}^2 {Q_{l,1(2)}}^2}, \tag{a14}$$

where $u_{1(2)}$ is the mode profile of the FW(SH) in the straight waveguide. Furthermore, we define the on-chip conversion efficiency as:

$$\eta_{\mathrm{on}} = \frac{P_{\mathrm{on2}}}{{P_{\mathrm{on1}}}^2} = \frac{P_{20} {\kappa_2}^2 {\kappa_1}^4}{{P_{\mathrm{in}}}^2}, \tag{a15}$$

where $P_{20}{\kappa_2}^2$ and $P_{\mathrm{in}}/{\kappa_1}^2$ are on-chip power of SH and FW, respectively. ${\kappa_{1(2)}}^2$ is the coupling coefficient between the waveguide and resonator, which can be calculated by the coupling Q quality with ${\kappa_{1(2)}}^2 = 2\pi(m_{1(2)} + M_{1(2)})/Q_{c,1(2)}$. So that η_{on} can be write in the form of

$$\eta_{\mathrm{on}} = \eta_{\mathrm{in}} \frac{8\pi^3 (m_{\mathrm{azi},2} + M_2)(m_{\mathrm{azi},1} + M_1)^2}{Q_{\mathrm{c},2} {Q_{\mathrm{c},1}}^2}. \tag{a16}$$

Finally, by separating ${f_2}{f_1}^2$ with other terms, dual-resonant on-chip conversion efficiency η'_{on} in the main-text can be obtained as well.